Technology in Cancer Research and Treatment
ISSN 1533-0346
Volume 10, Number 6, December 2011

Transrectal Ultrasound-Integrated Spectral Optical Tomography of Hypoxic Progression of a Regressing Tumor in a Canine Prostate

www.tcrt.org

Z. Jiang, Ph.D.[1#]
D. Piao, Ph.D.[1]*
K. E. Bartels, D.V.M./M.S.[2]
G. R. Holyoak, D.V.M./Ph.D.[2]
J. W. Ritchey, D.V.M./Ph.D.[3]
C. L. Ownby, Ph.D.[4]
K. Rock, D.V.M.[2]
G. Slobodov, M.D.[5]

[1]School of Electrical and Computer Engineering, Oklahoma State University, Stillwater, OK, USA
[2]Department of Veterinary Clinical Sciences, Oklahoma State University, Stillwater, OK, USA
[3]Department of Veterinary Pathobiology, Oklahoma State University, Stillwater, OK, USA
[4]Microscopy Laboratory, Oklahoma State University, Stillwater, OK, USA
[5]Department of Urology, University of Oklahoma Health Sciences Center, Oklahoma City, OK, USA
[#]Currently in Lightlab Imaging Inc., Westford, MA, USA

The objective of this study was to evaluate if transrectal optical tomography implemented at three wavelength bands for spectral detection could monitor changes of the hemoglobin oxygen saturation (S_tO_2) in addition to those of the total hemoglobin concentration ([HbT]) in lesions of a canine prostate, including an induced tumor modeling canine prostate cancer. Near-infrared (NIR) optical tomography was integrated with ultrasound (US) for transrectal imaging. Multi-spectral detection at 705 nm, 785 nm and 808 nm rendered measurements of [HbT] and S_tO_2. Canine transmissible venereal tumor (TVT) cells were injected into the right lobe of a dog's prostate gland, which had a pre-existing cyst in the left lobe. Longitudinal assessments of the prostate were performed weekly over a 63-day duration by NIR imaging concurrent with grey-scale and Doppler US. Ultrasonography revealed a bi-lobular tumor-mass regressing from day-49 to day-63. At day-49 this tumor-mass developed a hypoxic core that became larger and more intense by day-56 and expanded further by day-63. The tumor-mass presented a strong hyper-[HbT] feature on day-56 that was inconsistent with US-visualized blood flow. Histology confirmed two necrotic TVT foci within this tumor-mass. The cyst appeared to have a large anoxic-like interior that was greater in size than its ultrasonographically delineated lesion, and a weak lesional elevation of [HbT]. On day-56, the cyst presented a strong hyper-[HbT] feature consistent with US-resolved blood flow. Histology revealed acute and chronic hemorrhage in the periphery of the cyst. The NIR imaging features of two other TVT nodules and a metastatic lymph node were evaluated retrospectively. Transrectal US-integrated spectral optical tomography seems to enable longitudinal monitoring of intra-lesional oxygenation dynamics in addition to the hemoglobin content of lesions in the canine prostate.

Key words: Prostate cancer; Hypoxia; Optical tomography; Canine transmissible venereal tumor.

Introduction

Carcinoma of the prostate is a leading cause of death by cancer in American men (1). Effective management of locally advanced prostate cancer depends upon reliable and sensitive imaging of the degree of tumor oxygenation (2). For many solid tumors, including tumors in the prostate, hypoxia has been correlated with angiogenesis (3), tumor aggressiveness (4), local recurrence (5), and metastasis (6). Hypoxia also appears to be a prognostic factor in prostate cancer (7, 8). The relationship between prostate tumor oxygenation and response to

Abbreviations: Deoxygenated Hemoglobin (Hb); Diffuse Optical Tomography (DOT); Near-infrared (NIR); Oxygen Saturation (S_tO_2); Oxygenated Hemoglobin (HbO); Total Hemoglobin Concentration ([HbT]); Transmissible Venereal Tumor (TVT); Transrectal Ultrasound (TRUS); Ultrasound (US).

*Corresponding author:
D. Piao, Ph.D.
E-mail: daqing.piao@okstate.edu

radiation therapy has been well established (9), but hypoxia also affects and is affected by some chemotherapeutic agents (10). Although hypoxia is an important aspect of tumor physiology and response to treatment, the lack of simple and efficient methods to image oxygenation hampers further understanding and limits their prognostic usefulness (11). There is no 'gold standard' for hypoxia measurement (12). Eppendorf pO_2 histography (13) and immunohistochemical staining are considered invasive. Many noninvasive imaging technologies currently in clinical use rely on expensive equipment, and measurement of secreted markers provides an indirect measurement of hypoxia (11).

Near-infrared (NIR, 600-1000 nm) imaging is well-suited for non-invasive quantification of hemoglobin oxygen saturation (S_tO_2) (14). Since NIR light is strongly scattered by soft tissue, it is challenging to resolve S_tO_2 in deep tissue with high spatial resolution based on differentiating NIR absorptions by oxygenated and deoxygenated hemoglobin. Many recent studies on breast cancer imaging, however, demonstrated that the S_tO_2 information acquired non-invasively by NIR optical tomography in a suspicious lesion localized by high-resolution imaging modality such as MRI, ultrasound (US) effectively improved diagnosis, prognosis and treatment-monitoring of the cancer (15-17). For the prostate, there is limited information regarding optical characteristics of the prostatic tissue (18) as well as oxygenation of intact prostatic tissue (19). There has been no report of non-invasive optical imaging of S_tO_2 in neoplastic prostatic tissue in species that are comparative in size to the human prostate. A few studies investigated non-invasive optical imaging of NIR chromospheres such as hemoglobin in canine prostate by an approach of trans-rectal US-coupled optical tomography (20). For a rapidly growing canine transmissible venereal tumor (TVT) implanted in a canine prostate, a 3-fold increase of peak total hemoglobin concentration ([HbT]) in the tumor region over a 45-day duration was revealed by optical tomography implemented at 785 nm and 830 nm (21). To reliably recover S_tO_2, however, NIR measurement with a minimum of three wavelengths is required (22).

Given the plausibility of quantifying S_tO_2 in the prostate by triple-band trans-rectal optical tomography, to demonstrate its feasibility it is necessary to have a model of hypoxia in the animal prostate approximating the size of the human prostate. It is widely known that spontaneous and experimentally transplanted canine TVT in a non-immunocompromised host often shows an initial stage of rapid tumor growth, followed by a brief static period, and then a regressive stage that could become complete in adult dogs (23). The spontaneous regression of canine TVT is associated with an intense local lymphocytic infiltrate (24). This neoplasm has been used as a model to study the mechanisms of the tumor-specific immune response (25). Small blood vessels observed in canine TVT in the growth phase (26) correspond with the [HbT] elevation observed in a rapidly growing TVT (21). For a regressing canine TVT, the apoptotic degeneration and formation of connective tissue (26) could indicate interior hypoxic progression suitable for this study. However, the regression of canine TVT in a dog prostate was difficult to predict in the given time-frame of an experimental animal protocol due to many factors that may stimulate or inhibit host cell-mediated immune responses (27). In the current study, the TVT in the dog prostate did regress, which allowed trans-rectal optical tomography observation of tumor hypoxia in the canine prostate. Interestingly, this canine prostate was found, at baseline, to have a large cystic lesion located contra-lateral to the planned TVT implantation. Therefore, this dog, offered an unusual opportunity for observing the NIR oxygenation characteristics of a neoplastic lesion undergoing necrotic development and a native cystic lesion in the same prostate. Encountered in this study during gross-histology were also two additional TVT nodules and a metastatic lymph node, of which the retrospective NIR characteristics of [HbT] and S_tO_2 were different from those of the regressing TVT and the native cyst that were prospectively followed.

Materials and Methods

Transrectal US-Integrated Triple-Band Spectral Optical Tomography System

The transrectal US-integrated triple-band spectral optical tomography system is illustrated schematically in Figure 1. The system was developed based on an Aloka® transrectal ultrasound unit using a UST 672-5/7.5 bi-plane prostate probe containing a linear-array transducer for sagittal imaging at 7.5 MHz and a sector-array transducer for axial imaging at 5 MHz. The linear-array transducer was 60 mm long, providing a 60 mm field-of-view from the cranial to the caudal aspects on sagittal imaging. On the lateral sides of the linear-array transducer, which was 10 mm wide, were an optical source-array and an optical detector-array separated 20 mm laterally from each other and symmetric to the linear-array ultrasound transducer. Each of the optical source-array and the detector array had 7 channels evenly distributed along the 60 mm length, so the optical array was aligned parallel to the linear-array ultrasound transducer. A rectangular aperture was opened on the substrate of the optical array for exposing the linear-array ultrasound transducer. Each channel of the source-array or detector-array contained a micro prism-lens pair of 1 mm size coupled to a metal-coated multi-mode fiber, for side light delivery to or collection from the tissue.

The outputs of three laser diodes (LDs) at 705 nm, 785 nm, and 808 nm wavelengths, respectively, were combined by a tri-furcated fiber bundle (FiberTech Optica Inc.). The triple-band light exiting the fiber bundle was then collimated to one of the 7 channels of the optical source-array, by a

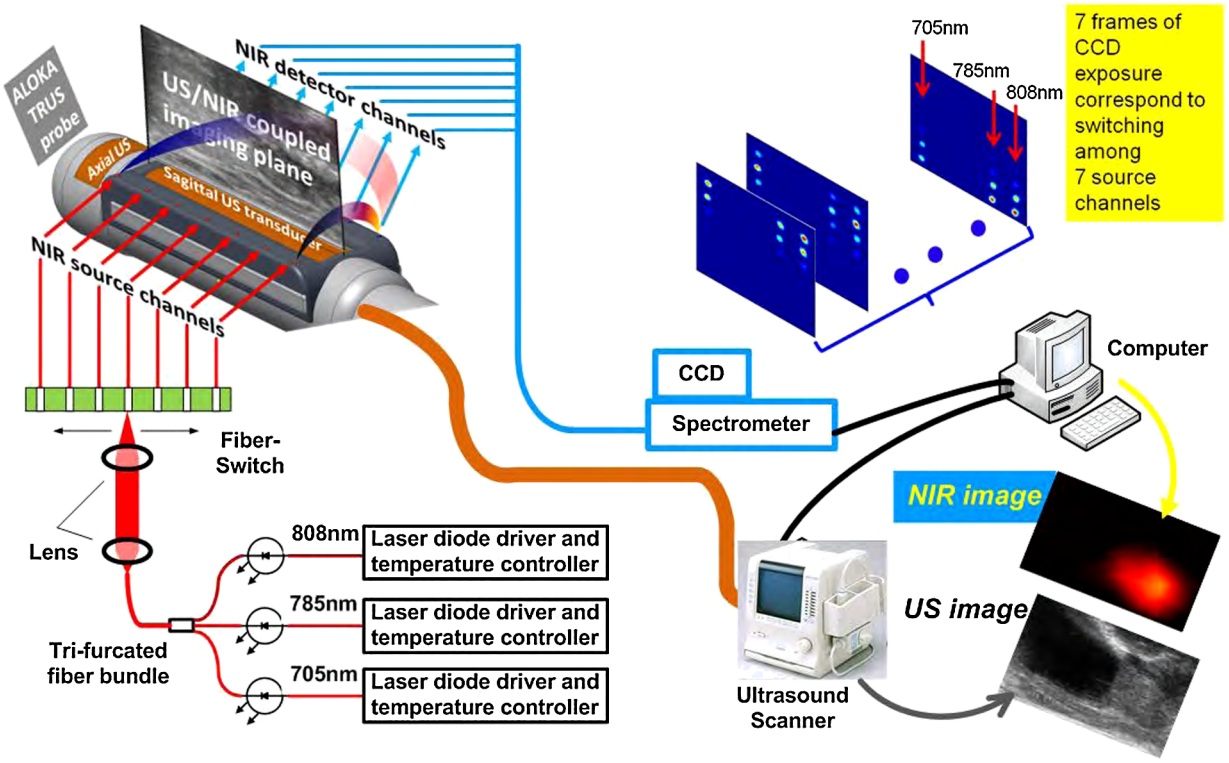

Figure 1: Schematic diagram of the system and data-acquisition flow of trans-rectal US-integrated triple-band optical tomography.

home-built fiber switch developed upon a linear motorized translation stage (Ziber Technology). The 7 channels of the optical detector-array were aligned vertically at the entrance slit of a spectrograph (Princeton Instruments) with a 300-mm focal-length, for the triple-band light to be dispersed by a 300 grooves/mm grating onto a CCD camera-chip (Princeton Instruments) of 12.0 mm × 12.0 mm. The system's parameters allowed a spectral coverage of approximately 110 nm, therefore LDs of 705 nm, 785 nm, and 808 nm were chosen from models available to this study.

Conventionally a dual-wavelength combination with one wavelength 10 s of nanometer below and the other wavelength 10 s of nanometer above the isosbestic point (805 nm) of hemoglobin could be implemented for extracting the hemoglobin oxygenation information. However, Zhu suggested (22) that even though two wavelengths in the opposite neighborhoods of the isobestic point were quite accurate in recovering the [HbT], they were less reliable in quantifying S_tO_2, which could be attributed partially to the error introduced by neglecting water or lipid. Therefore the recommendation had been to implement one additional shorter wavelength that is much distant from the isobestic point to form essentially a three-wavelength configuration to recover two unknowns of HbO and Hb, not only for minimizing the error introduced by water or lipid, but also for improving the sensitivity to the changes in hemoglobin oxygenation, as the difference between the absorptions of deoxygenated hemoglobin (Hb) and oxygenated hemoglobin (HbO) became greater toward short-wavelength than in the longer wavelength in the near-infrared band. The 705 nm LD was therefore chosen in this study along with the 785 nm LD available in the previous 2-wavelength setup (21), but the limited spectral coverage of the spectrograph-CCD set forced us to use an 808 nm LD and abandon the 830 nm LD available in the previous 2-wavelength setup. It is certainly anticipated that using a LD with a wavelength more sensitive to the changes of HbO, *i.e.,* 835 nm, in addition to using a LD with a wavelength more sensitive to the changes of Hb, *i.e.,* 785 nm, in the triple-band configuration could further improve sensitivity and accuracy of measuring the hemoglobin oxygenation.

For each channel of the optical source-array, a single frame of the triple-band signal was acquired by the CCD, and the acquisition of 7 frames corresponding to all 7 channels of optical source-array were completed in 4 seconds through a LabVIEW (National Instruments) routine to synchronize the CCD exposure with the fiber-switching among the source channels. The 7 frames of data corresponding to one complete set of imaging were post-processed for absorption tomography (21) followed by derivations of [HbT] and S_tO_2 maps as given in more detail in the following section. Ultrasound images were acquired prior to the starting of the NIR data acquisition by a frame-grabber installed in the

control-computer, and used for correlating with the reconstructed NIR images.

Triple-Band Spectral Optical Tomography Measurements of [HbT] and S_tO_2

The parallel-linear geometry of the optical source-array and detector-array entails 3-dimensional optical tomography reconstruction; however, due to the 2-dimensional ultrasonography only the middle sagittal image of optical tomography has an ultrasound image to correlate with. The optical tomography reconstruction was performed in a volume of 80 mm × 70 mm × 50 mm (cranial-to-caudal × right-lateral-to-left-lateral × dorsal-to-ventral), and a 60 mm × 40 mm view of middle sagittal image of optical tomography was extracted to correlate with the middle sagittal ultrasound image of the same dimension, as detailed in Figure 2A. Note that the maximum longitudinal view of the ultrasound image was 60 mm, and the depth of the ultrasound image could reach much greater than 40 mm. However, as the geometry of optical array allowed an imaging depth in the range of 20-30 mm (approximately 1/3—1/2 of the dimension of the array), the information of optical tomography beyond 40 mm would be unreliable. The dimension of optical tomography reconstruction was, however, made substantially greater than the dimension of the image actually extracted for correlating with ultrasound, for the need in accommodating the medium conditions in the volume confined by the virtual boundary in the reconstruction.

The system utilized steady-state optical tomography reconstruction for absorption tomography (28, 29). The absorption coefficients at the three specific bands ($\mu_a^{\lambda_1}$, $\mu_a^{\lambda_2}$ and $\mu_a^{\lambda_3}$) were recovered first, then used to calculate the concentrations of HbO and Hb, by

$$\begin{bmatrix} \text{HbO} \\ \text{Hb} \end{bmatrix}_{2\times1} = \frac{1}{\ln(10)} \cdot \left\{ \frac{1}{[\varepsilon]'[\varepsilon]} \right\}_{2\times2} \cdot [\varepsilon]'_{2\times3} \cdot \begin{bmatrix} \mu_a^{\lambda_1} \\ \mu_a^{\lambda_2} \\ \mu_a^{\lambda_3} \end{bmatrix} \quad [1]$$

where $[\varepsilon]_{3\times2}$ was the matrix of the molar extinction coefficients represented by

$$[\varepsilon]_{3\times2} = \begin{bmatrix} \varepsilon_{\text{HbO}}(\lambda_1) & \varepsilon_{\text{Hb}}(\lambda_1) \\ \varepsilon_{\text{HbO}}(\lambda_2) & \varepsilon_{\text{Hb}}(\lambda_2) \\ \varepsilon_{\text{HbO}}(\lambda_3) & \varepsilon_{\text{Hb}}(\lambda_2) \end{bmatrix} \quad [2]$$

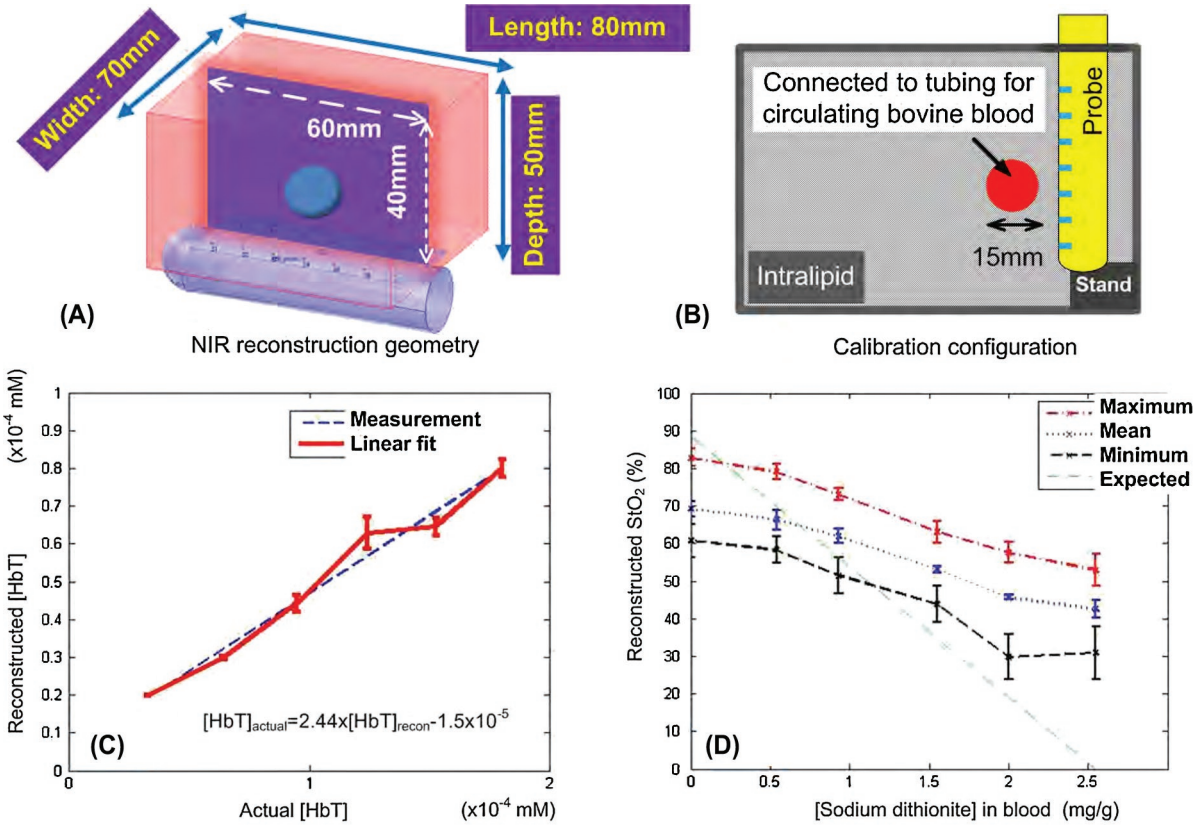

Figure 2: Information related to the imaging geometry and calibration of [HbT] and S_tO_2 measurement. (**A**), Optical tomography performs 3-D reconstruction in the shown cubic geometry, with the middle sagittal plan correlating to sagittal ultrasound. (**B**), Experimental configuration for measuring the blood content in a tissue-mimicking container. (**C**), Measured [Hb] versus actual [HbT] shows a good linear relationship. (**D**), Measured S_tO_2 varies in a range, with the decreasing trend not as significant as that predicted from the concentration of the chemical in the blood sample.

and $[\varepsilon_x(\lambda)]$ denoted the molar extinction coefficient of the specified chromophore X. The calculated [HbO] and [Hb] were then used to derive [HbT] in the unit of millimole (mM) by [HbT] = [HbO] + [Hb] and S_tO_2 in the unit of percentage (%) by S_tO_2 = [HbO]/[HbT] × 100.

A direct reconstruction method has been demonstrated to recover the chromophore concentrations without going through the reconstruction of wavelength-specific absorption coefficients (30). That method is shown robust, however the advantage of it over the conventional indirect reconstruction method may depend upon sufficient numbers of optimal wavelengths. We have tested the direct reconstruction method for the three wavelengths used in this system, and found the outcome inferior to the indirect method implemented here.

The calibration setup for measuring [HbT] and StO_2 is shown in Figure 2B. The US-integrated optical-array probe was vertically positioned in a tank of bulk intralipid solution. A thin-wall cylindrical container with 15 mm outside diameter and 40 mm length, made of tissue-mimicking phantom material (21), was positioned orthogonal to the optical-array probe. The center of the cylindrical container was placed approximately 20 mm from the middle-portion of the optical-array probe. This cylindrical container was connected to a blood-bank outside the tank through Teflon tubing for circulating the blood. Fresh bovine blood diluted with saline water to different concentrations (31) was used to calibrate the measurement of [HbT]. As shown in Figure 2C, a linear-relationship observed between the reconstructed and actual values of [HbT] was used to convert [HbT] values in the *in vivo* measurements. For the evaluation of S_tO_2 reconstruction, an oxygen-regulating chemical, Sodium-Dithionite (32), was mixed in the fresh bovine blood. The reconstructed StO_2 values decreased as the concentration of the Sodium-Dithionite increased, for different distances of the cylindrical container from the optical-array probe (moving 5 mm to or from the probe with respect to the center-position of 20 mm). However, the decreasing trend was not strong enough as compared to the very-limited published empirical trails. The discrepancy could have resulted from a number of other factors, including the abrupt change of optical properties in the cylindrical container with respect to that in the background medium (29). For *in vivo* measurements, the tissue volume being imaged likely would have a smooth change of optical properties that likely would give rise to better recovery of S_tO_2, therefore for *in vivo* measuring the reconstructed S_tO_2 were used directly instead of going through a conversion between the measured and the expected values as with [HbT] measurements. Note that even through the S_tO_2 information may not be quantitatively accurate, the qualitative S_tO_2 features could still render important contrasts of tissue oxygenation.

Animal Model and Imaging Protocol

The Institutional Animal Care and Use Committee of Oklahoma State University approved this study. An adult 27-kg, intact male, foxhound estimated to be seven years of age was used. The canine TVT cells were propagated in non-obese-diabetic/severe-combined-immunodeficiency (NOD/SCID) mice and recovered/homogenized for injection into the canine prostate gland parenchyma without immune-suppression. Under general anesthesia, a 6-inch 16-gauge hypodermic needle was introduced aseptically and transperineally into the right lobe of the prostate, using palpation and US visualization. After retracting the stylet, ~2 cc suspension of 2.5×10^6 cells/mL TVT cells were injected into the right prostatic lobe near the cranial edge of the gland as shown in Figure 3A, then the stylet was re-placed in the needle for minimizing seeded tumor along the needle-track during needle retraction. The dog was then monitored by transrectal digital palpation, transrectal grey-scale and Doppler US, and optical tomography at weekly intervals over a 63-day period.

The base-line examination including US indicated a prostate that presumably had benign prostatic hypertrophy and measured 7.0 cm cranial-to-caudal. The base-line US also revealed a large cystic lesion in the left lobe (see Figure 3B for schematic location and D for US image of the cystic lesion). The cyst extended irregularly within the left mid-lateral aspect of the prostate, and had a "scorpion" like shape on some sagittally acquired US images (see Figure 3F). There were no remarkable findings in the mid-lateral aspect of the right prostatic lobe on the base-line US, (see Figure 3E). After introducing the TVT emulsion into the right lobe, the injection site was noticeable on US as indicated by the red arrow in Figure 3C. Although the injection was locally-confined, it has been expected that the TVT growth in prostate could occur at locations different from the injection site (20, 21), due to the round-cell natural of the TVT cells, the ductal morphology of the prostate gland and the metastatic potential.

For all baseline and post-injection examinations, transrectal US-integrated optical tomography was performed on five quasi-sagittal planes (Figure 3B), including the middle-sagittal, half-way to the right lateral edge, the right lateral edge, half-way to the left lateral edge, and the left lateral edge of the prostate gland for "laterality" evaluation. On each of the five quasi-sagittal planes the imaging was performed at three longitudinal positions of the optical-array probe with respect to the prostate. For the case of middle-sagittal plane, at the longitudinal position 1 the imaging field-of-view covered the cranial edge of the prostate with the bladder visible, at the longitudinal position 3 the imaging field-of-view covered the caudal edge of the prostate, and the longitudinal position 2 was in between the longitudinal positions 1 and 3. Such

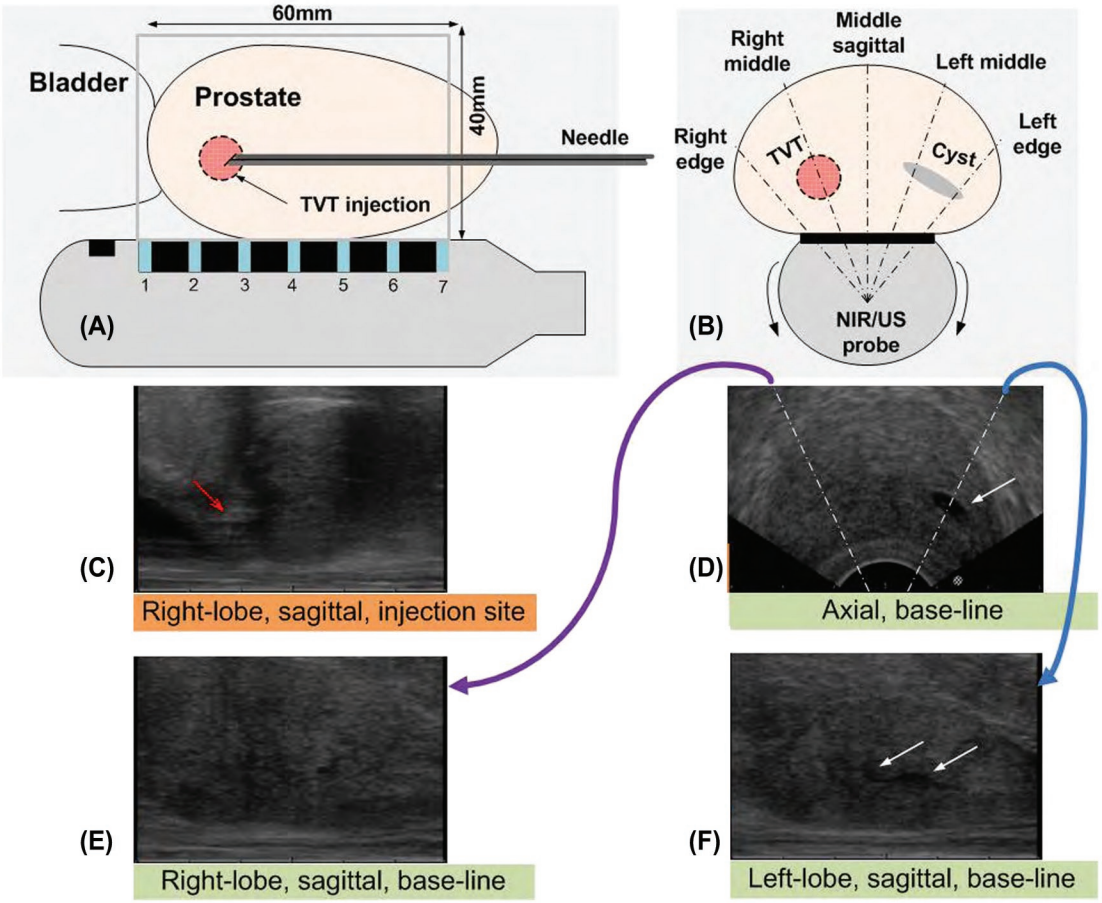

Figure 3: The study was conducted on a dog that had a naturally occurring cystic lesion in its left lobe. Order of sub-figures: clockwise from the upper-left. (**A**) and (**B**), imaging geometry; (**D**) and (**F**), a large "scorpion-like" cystic lesion extending irregularly within the left lobe; (**E**), the right lobe was unremarkable on the base-line US; (**C**), the TVT injection site in the right lobe was noticeable on US as indicated by the red arrow. White solid arrow: cystic lesion.

measurements were necessary for cross-validation of the NIR imaging features associated with each quasi-sagittal plane.

At each location of the optical-array probe, the sequence of image visualization and data acquisition includeded: grey-scale ultrasonographic evaluation followed by acquisition of the grey-scale US frame by the control-computer, turning on color-Doppler mode in US followed by acquisition of the Doppler US frame (sometimes two frames of Doppler US were acquired as the cranial-caudal field-of-view of Doppler was about ½ of that of gray-scale US), and 3 sets of repeated NIR data acquisition (each set containing the 7 frames of CCD data as illustrated in the upper-right corner of Figure 1). Note that the NIR data acquisition was not gated by the anesthesia instrument, so the 4-seconds NIR data acquisition could have had interference from the breathing of the dog, as well as possible movements or shifts of the hand-held transrectal probe during each cycle of NIR data acquisition.

Gross and Microscopic Examination

On day-63, the dog was humanely euthanized using a barbiturate overdose. A complete necropsy was performed that included a thorough gross inspection and excision of the prostate gland, urinary bladder and pelvic lymph nodes. The prostate was serially sectioned using a freehand technique in quasi-sagittal planes approximating those used for weekly monitoring by transrectal US and NIR imaging. Routine histology with hematoxylin and eosin (H&E) stain was performed on specimens selectively sampled from the sectioned prostate, each of which contained tissues that were grossly expected to be normal, cystic, neoplastic, or necrotic, and the excised lymph nodes.

Results

Shown in Figure 4 are the images acquired at base-line, days 49, 56 and 63 after the TVT injection, of Doppler-overlapped US, grey-scale US, and optical tomography of [HbT] and S_tO_2, at left-mid-sagittal plane across the cystic lesion (upper panel) and right-mid-sagittal plane across the planed TVT injection site as well as a later developed hypo-echoic mass (lower panel). As the Doppler-overlapped US was recorded after grey-scale US, slight differences may be observed between anatomies shown on the two US images.

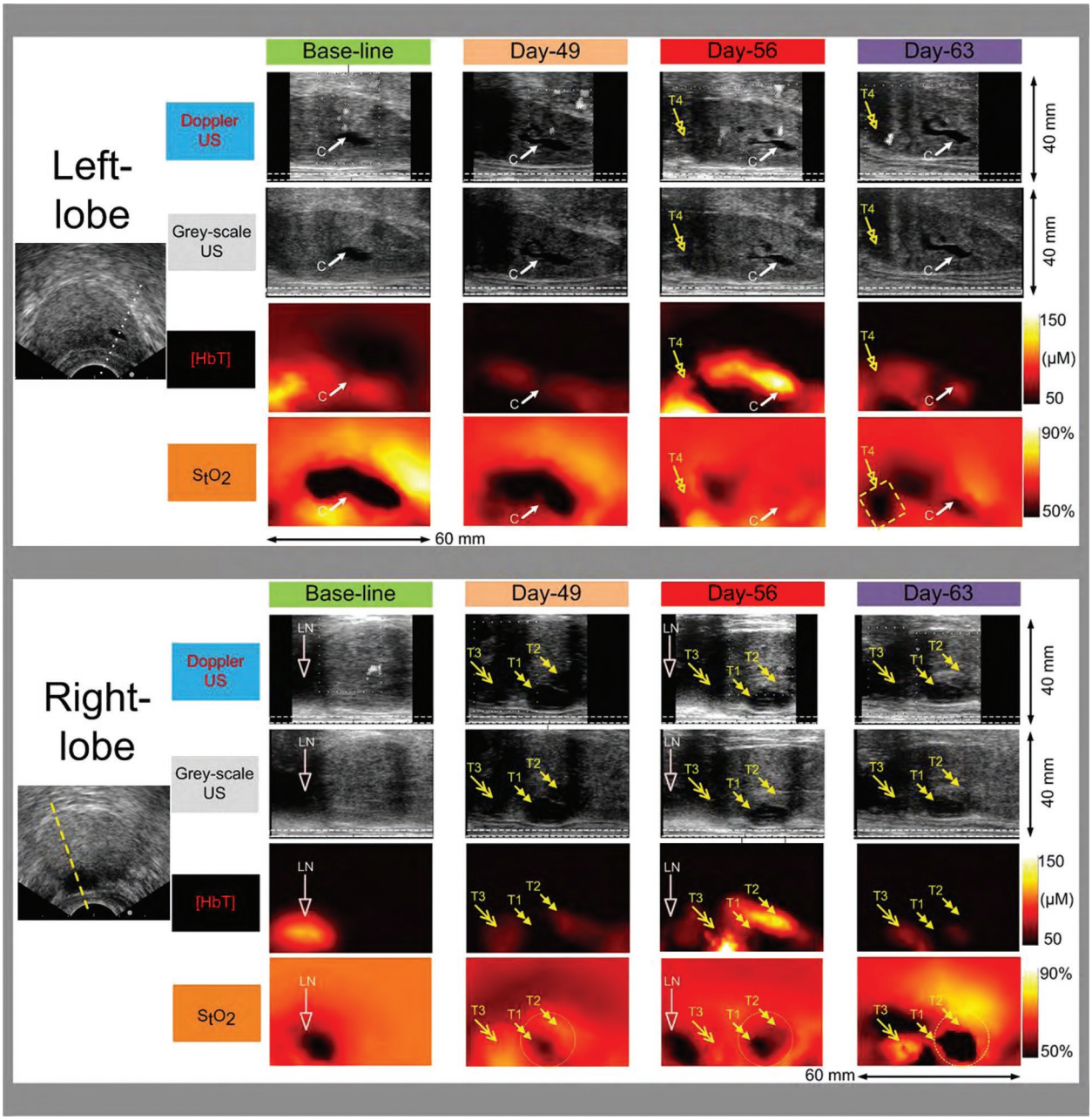

Figure 4: Image dimension—60 mm × 40 mm (cranial-caudal × dorsal-ventral). Images were acquired at base-line, day-49, day-56 and day-63 after the injection, for Doppler US, grey-scale US, [HbT] and S_tO_2, at left-mid-sagittal plane across the cyst (marked by the dotted line across the axial US image in the upper panel for the left-lobe) and right-mid-sagittal plane across the planed TVT injection site as well as a later developed tumor mass (marked by the dashed line across the axial US image in the lower panel for the right-lobe). The dashed line at the dorsal edge of the US images indicates the actual location of the NIR sensors at approximately 3 mm ventral to the surface of the US transducer. The color-scales for NIR images are (50-150) μM for [HbT] and (50-90)% for S_tO_2, respectively. C indicates cyst; LN indicates lymph node; T indicates tumor.

Baseline

At baseline, the right prostatic lobe had homogenous S_tO_2 and [HbT] ≤50 μM, except for a hypo-echoic region with indistinct ultrasonographic margins at the right-cranial edge of the prostate that was indicated in NIR images as having a "bean-shape" of 10 mm × 20 mm in axes, with clear hyper-[HbT] and hypo-StO_2 contrasts. This region was consistent with a lymph node (marked by "LN"). Comparatively, the left prostatic lobe had a large anoxic-like region extending longitudinally and corresponding to the irregular gross profile of the cystic lesion (marked by "C") on US. That anoxic-like region presented slightly elevated but relatively homogenous [HbT].

Right-Lobe

After TVT injection in the near-cranial-edge of the right lobe, the development of a hypo-echoic mass in the middle-aspect of the right lobe became evident on US by day-28, and was indicated approximately 1-week earlier on NIR as having locally-increased [HbT]. By day-49 the mass in the middle-aspect of the right lobe (marked by "T1" and "T2") turned to an anechoic and bi-lobular structure with shadowing at its caudal aspect. The larger dorsal-cranial-mass "T1" had a hypoxic focus and unremarkable [HbT] contrast; the smaller ventral-caudal-mass "T2" had weakly-marked S_tO_2 contrast and weakly increased [HbT]. By day-56, T1 reduced slightly in size on US with echoic reverberation artifact, the hypoxic focus of it becoming larger and more intense, and the [HbT] contrast of it remaining undetectable. Comparatively, T2 was unremarkable on US except for the shadowing hypoechoic region at the caudal aspect of the previously-indicated mass, the focus of it appearing as slightly hypoxic and having significantly increased [HbT]. By day-63, T1 remained unchanged in size on US with reduced echoic reverberation artifact, and the caudal aspect of the T2-indicating region became heterogeneously hypo-echoic without shadowing. The extended region corresponding to T1&T2 was mostly anoxic-like, and only weak hyper-[HbT] contrast was observed in the indicated T2 mass. Quantitatively, within a spherical region of 20 mm in diameter centering on the sagittal plane of the right-lobe in Figure 4 and enclosing T1&T2 (marked by the dashed circle), the minimum S_tO_2 dropped from 49% in week-7 to 20% in week-9, and the volume of S_tO_2 below 50% increased from 0.05 cm^3 in week-7 to 1.95 cm^3 in week-9. The changes of these two aspects of S_tO_2 within the circled region from week-7 to week-9 are plotted separately at the bottom panel of Figure 5.

By day-63 a nodular structure was also observed on S_tO_2 image at a location (marked by "T3") cranial to the "T1&T2" region. T3 appeared as non-hypoxic with weak heterogeneous elevation of [HbT]. Retrospectively, on day-56 a nodular structure at the indicated location of T3 was difficult to resolve except for an irregular strongly hyper-[HbT] region correlating longitudinally to the indicated location of T3. On day-49 the indicated T3 region was essentially iso-oxic and had weak homogenous elevation of [HbT]. On grey-scale US the indicated T3 region was hypoechoic with shadowing from day-49 to day-63, but unremarkable on Doppler US. On US it was difficult to evaluate whether T3 was confined within the prostatic capsule. Besides T1, T2, and T3, on day-56 a "bean-shape" structure was visible on S_tO_2 image, and it was similar in location, shape and size to the one lymph node-like structure shown at base-line, but with slightly stronger hypoxic interior and much weaker [HbT] contrast.

Left-Lobe

By day-49 the cystic lesion remained similar in NIR appearances to that in base-line. On Doppler US the blood flow was observed in areas ventral to the cystic lesion. By day-56, it presented strong heterogeneously elevated [HbT] of which the gross profile resembled the hypoxic profile of the cystic lesion in base-line and day-49. The region of strong heterogeneously elevated [HbT] was associated with weak heterogeneous hypoxia. On Doppler US the blood-flow was observed at the cranial and mid-caudal aspects of the cystic lesion that correlated longitudinally with the hyper-[HbT] region. By day-63, the cystic lesion appeared as having weak lesion-wise hyper-[HbT] and heterogeneous hypoxic interior, both were comparative in size to the ultrasonographically delineated lesion. On Doppler US the blood flow was observed in areas ventral to the cystic lesion, however, no consistent feature in the proximity of the cystic lesion indicating lesion-wise blood flow was observed.

By day-63, a hypoechoic mass with shadowing and Doppler flow-signal in its caudal aspect was noticed at the cranial-dorsal edge of the left lobe and was seemingly confined within the prostatic capsule (marked by "T4"). At the indicated position of T4 mass, a hypoxic region of approximately 10 mm in longer axis was seen on S_tO_2 image with weak hyper-[HbT] contrast. Retrospectively on day-56, the T4 mass was shown smaller on US with shadowing, and at its dorsal aspect heterogeneously elevated [HbT] and S_tO_2 contrast were noticed.

Gross Examination

Gross examination (Figure 5) found the prostate measured approximately $8 \times 5 \times 5\,cm^3$. TVT metastases were found in four peri-prostatic lymph nodes, among which the right peri-prostatic lymph node (pointed by "LN") measured approximately 10 mm × 20 mm in axes.

The excised prostate was sliced in the quasi-sagittal orientations approximating those used for weekly monitoring, as indicated by the dashed lines in the axial US images in Figure 5. The right lobe contained solid tumor-mass in the middle-dorsal aspect of the gland that extended across the midline. This solid mass, circled and pointed by "T1&T2", had two dark foci evident for necrosis. Cranial to this necrotic region was a nodule indicating a neoplastic tissue-mass. The location, shape and size of this neoplatic nodule were consistent with those of T3 identified on S_tO_2 image by day-63 in Figure 4.

The left lobe contained a cyst that extended irregularly in both longitudinal and lateral directions within the left-middle-caudal aspect of the gland, and filled with fluid. A nodule of approximately 8 mm in longer-axis was found at

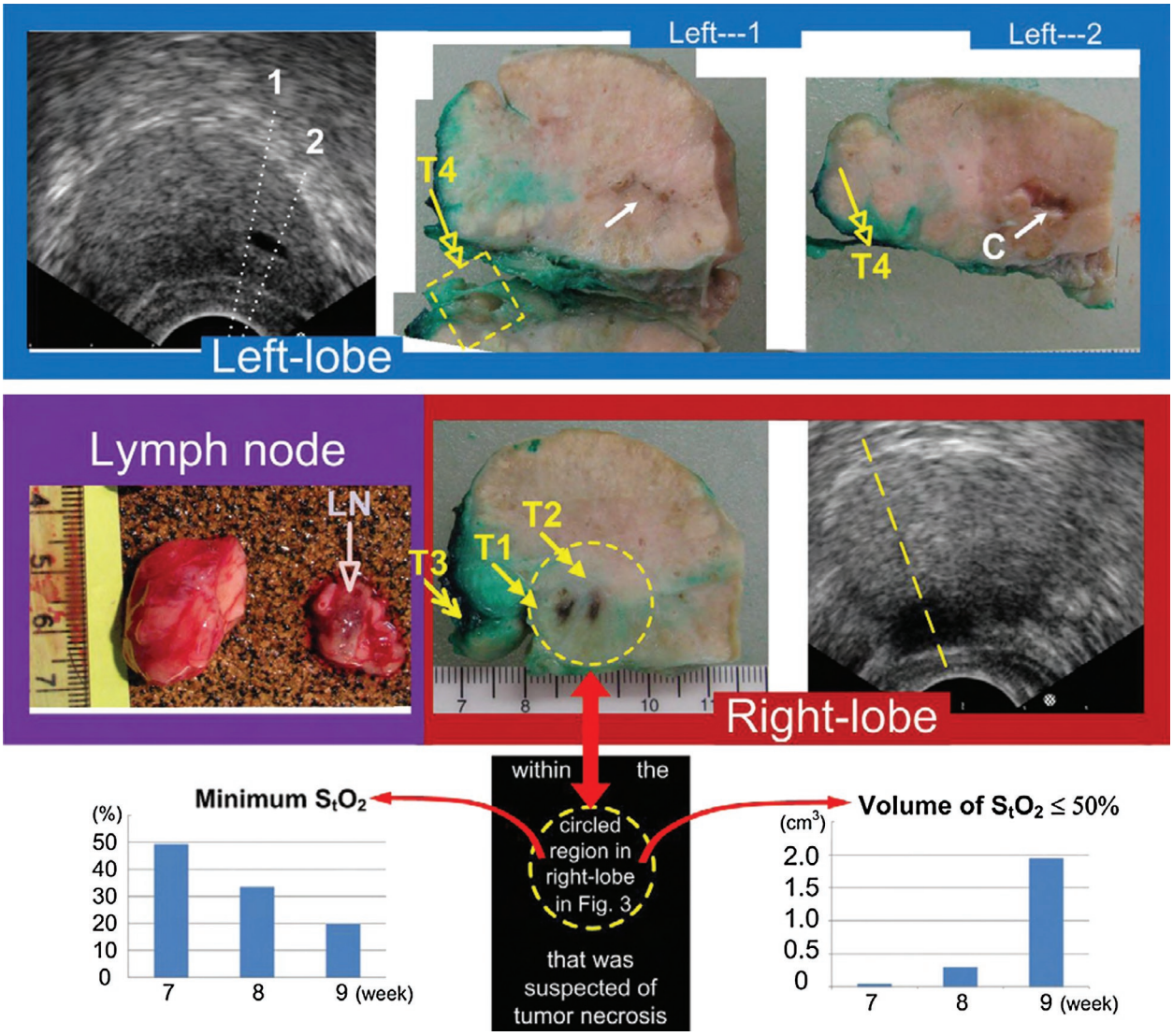

Figure 5: Top-panel: left-lobe. Middle-left-panel: lymph node. Middle-right-panel: right-lobe. Bottom panel: the minimum S_tO_2 and volume of S_tO_2 less than 50% within the circled region in the right-lobe in Figure 4 that enclosed the foci of tumor undergoing necrotic development from week-7 to week-9.

an intra-capsular position (enclosed by the dashed rectangle pointed by "T4") near the dorsal-cranial edge of the left-lobe on the quasi-sagittal plane intersecting the medial edge of the cyst. The location, size, and shape of it resembled those of T4 identified on S_tO_2 image by day-63 in Figure 4. The gross character of the "T4" mass was unmistakable for a TVT.

Light Microscopy

The H&E histology results are given in Figure 6. In the right lobe, foci of necrosis were confirmed within the TVT mass encircled in Figure 5. In the right peri-prostatic lymph node, TVT infiltration with remnant cortical lymphocytes was found. In the left-lobe, numerous tufts of new capillaries, acute hemorrhage and hemosiderophages indicating chronic hemorrhage were found in the tissue surrounding the cyst.

Summary of the Imaging and Histology Evaluations

Among the six lesions evaluated, T1&T2 were evaluated prospectively but clarified retrospectively, C was followed prospectively, T3, T4, and LN were identified retrospectively. For a summary, the imaging features of each are presented respectively in the Tables I to VI.

Discussions

Some NIR imaging characteristics were difficult to correlate with ultrasonography due to breathing movements of the

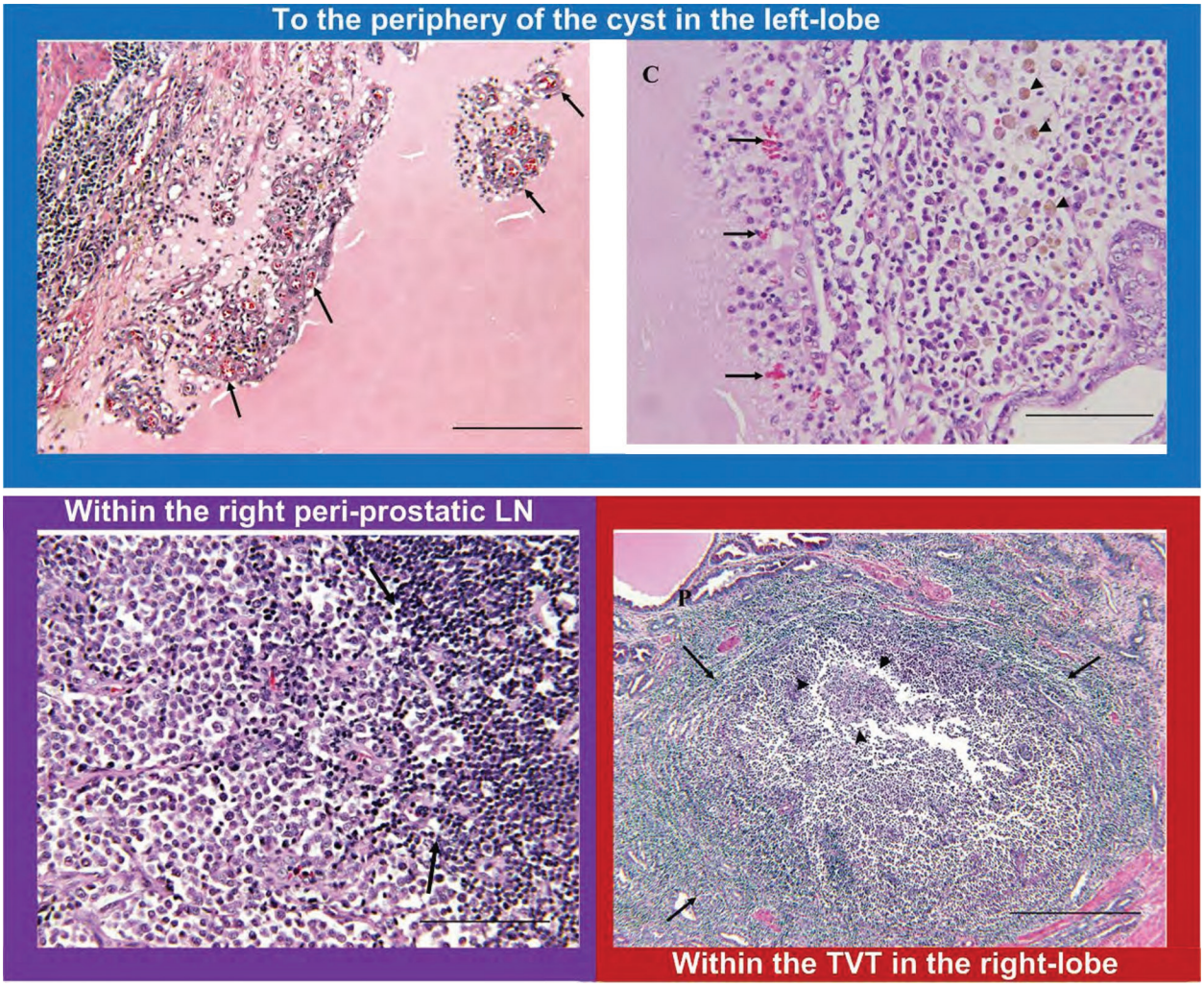

Figure 6: Top-left: Numerous tufts of new capillaries (arrows) surrounding the prostatic cyst. Bar = 200 um. Top-right: Acute hemorrhage (arrows) and hemosiderophages indicating chronic hemorrhage (arrowheads) in tissue surrounding the cyst. (C) cyst lumen. Bar = 100 um. Lower-left: TVT effacing lymph node. Arrows delineate TVT infiltrate (left side) with remnant cortical lymphocytes (right side). Bar = 100 um. Lower-right: Focus of necrosis within TVT mass in the middle-aspect of the right lobe. Prostatic tissue (P). Portion of TVT mass outlined by arrows. Central focus of necrosis outlined by arrowheads. Bar = 500 um.

subject as well as shift of the trans-rectal applicator between US frame and NIR data acquisition. Nevertheless, this single-case retrospective study demonstrated longitudinal NIR image-monitoring of naturally-occuring cyst and experimentally-induced neoplastic lesions in a canine prostate.

It has been well documented that TVT regression is secondary to development of a host, tumor-specific immune response. This study demonstrated a decrease in oxygen level in the tumor-regressing area, likely due to cellular degeneration, lysis and extensive debris (24). In this study, the T1 mass of the bi-lobular TVT structure progressed steadily from weakly hypoxic by day-49 to extensively hypoxic by day-63, with insignificant changes in its [HbT]. In comparison, the hypoxic progression of the T2 mass of the bi-lobular TVT structure was associated with strong intermittent elevation of [HbT] by day-56 in the lesion area. As blood-flow in the T2 region was not evident on Doppler US by day-56, the NIR-indicated lesion-wise elevation of [HbT] in this regressing tumor suggested an increase of tumor micro-vasculature secondary to an early fibrovascular reparative response (granulation) following tumor regression (33). By day-63, the hypoxic focus of T1&T2 was distinct, and a hypoxic interior was obvious in T4 but not in T3, all suggesting that the TVT nodules had entered the regression phase non-simultaneously or regressed at different rates. For the LN, the "bean-shape" appearance of it on base-line NIR images strongly suggested a nodular-vasculature agreeing with lymph-node anatomy, and the strong reduction of nodal-wise [HbT] coupled with slightly intensified low-S_tO_2 contrast by day-56 over base-line could signal tumor metastasis (34).

Table I
Summary of imaging features observed from T1.
←(***prospectively evaluated as well as retrospectively clarified***)→

	Baseline	Day-49	Day-56	Day-63	Gross Histology	Light Microscopy
US------Doppler	N/A	Indistinct	Indistinct	Indistinct	Solid tumor mass, one of two dark foci indicating necrosis	Necrosis
US---Grey Scale	N/A	Anechoic	Anechoic, size reduced	Anechoic. Size unchanged		
NIR---[HbT]	N/A	Unremarkable	Undetectable	Undetectable		
NIR---S_tO_2	N/A	Hypoxic focus	Hypoxic focus larger and more intense	Anoxic-like, extending to T2		

Table II
Summary of imaging features observed from T2.
←(***prospectively evaluated as well as retrospectively clarified***)→

	Baseline	Day-49	Day-56	Day-63	Gross Histology	Light Microscopy
US------Doppler	N/A	Indistinct	Indistinct	Indistinct	Solid tumor mass, one of two dark foci indicating necrosis	Necrosis
US---Grey Scale	N/A	Anechoic	Isoechoic	Heterogeneously hypoechoic		
NIR---[HbT]	N/A	Hyper, weak	Hyper, strong	Hyper, weak		
NIR---S_tO_2	N/A	Weakly marked	Hypoxic, weak	Anoxic-like, extending to T1		

Table III
Summary of imaging features observed from C.
(***prospectively evaluated***)→

	Baseline	Day-49	Day-56	Day-63	Gross Histology	Light Microscopy
US------Doppler	Blood flow ventral to the cyst	Blood flow ventral to the cyst	Blood flow in the extended cystic region	Blood flow ventral to the cyst	Irregularly shaped cystic lumen filled with fluid	Acute hemorrhage chronic hemorrhage
US---Grey Scale	Anechoic	Anechoic	Anechoic	Anechoic		
NIR---[HbT]	Hyper, weak indistinct shape	Hyper, weak indistinct shape	Hyper, strong heterogeneous	Hyper, weak		
NIR---S_tO_2	Anoxic-like, distinct shape and margin	Hypoxic, strong distinct shape and margin	Hypoxic, slight, in-distinct shape and margin	Hypoxic, weaker, less-distinct shape and margin		

Table IV
Summary of imaging features observed from T3.
←(***retrospectively identified***)

	Baseline	Day-49	Day-56	Day-63	Gross Histology	Light Microscopy
US------Doppler	N/A	Unremarkable	Unremarkable	Unremarkable	Nodule indicating a neoplastic tissue mass	N/A
US---Grey Scale	N/A	Hypoechoic	Hypoechoic	Hypoechoic		
NIR---[HbT]	N/A	Hyper, weak	Hyper, strong	Hyper, heterogeneous, weak,		
NIR---S_tO_2	N/A	undetectable	Indistinct	Distinct nodular shape		

Table V
Summary of imaging features observed from T4.
←(***retrospectively identified***)

	Baseline	Day-49	Day-56	Day-63	Gross Histology	Light Microscopy
US------Doppler	N/A	N/A	Unremarkable	Flow caudal to the lesion	Unmistakable for a TVT mass	N/A
US---Grey Scale	N/A	N/A	Hypoechoic	Hypoechoic		
NIR---[HbT]	N/A	N/A	Hyper, heterogeneous	Hyper, weak		
NIR---S_tO_2	N/A	N/A	Hyper, heterogeneous	Hypoxic, indistinct shape and margin		

The lesion profiles of T1, T2, T3, T4, and LN indicated on S_tO_2 images were comparable to those identified ultrasonographically. For the cyst, however, the hypoxic region seemed to noticeably outsize the ultrasonographically delineated lesion in most images. This could be due to insuffient image resolution of NIR compared to US; however, it could also indicate that NIR detection of S_tO_2 characteristics was able to resolve the viability gradient of peri-cystic tissue non-detectable by ultrasonography. The latter indication agrees with a study of optical imaging of the breast suggesting that

Table VI
Summary of imaging features observed from LN.
←(***retrospectively identified***)

	Baseline	Day-49	Day-56	Day-63	Gross Histology	Light Microscopy
US------Doppler	N/A	N/A	N/A	N/A	Abnormal morphology suspected of TVT metastasis	TVT infiltration with remnant cortical lymphocytes
US---Grey Scale	Hypoechoic, indistinct margin	N/A	Hypoechoic	N/A		
[HbT] contrast	Hyper, strong distinct bean-shape	N/A	Hyper, weak indistinct bean-shape	N/A		
S_tO_2 contrast	Hypoxic, strong distinct bean-shape	N/A	Hypoxic, strong distinct bean-shape	N/A		

the spatial extent of optical contrast in breast tumors may be significantly greater than anatomical dimensions reported by standard imaging modalities including ultrasound (35). NIR imaging also revealed weakly elevated peri-cystic [HbT] when no blood flow was detectable on Doppler-US. Chronic intra-lesional hemorrhage found in the cyst (36) supported the slight [HbT] elevation that was resolvable by NIR but not by Doppler-US. On day-56 strong lesion-wide elevation of [HbT] was observed in the area corresponding to the entire cystic lesion; whereas blood flow on Doppler-US was detected only exterior to the ultrasonographically marked lumen. Acute intra-lesional hemorrhage found 7-day later implied that the lesion-wide strong (Hb) elevation along with weak hypoxic interior was likely due to edema (37) around the cyst that could be secondary to the tumor regression in the contra-lateral lobe.

Conclusion

This study evaluated transrectal US-integrated spectral optical tomography of S_tO_2 and [HbT] of lesions in a canine prostate. The hypoxic focus of a regressing canine TVT tumor was found to become larger and more intense over the course of regression leading to necrosis. The cyst usually appeared to have a large anoxic-like interior that was greater in size than its ultrasonographically delineated lesion, and weak lesion-wise elevation of [HbT] that correlated with intra-lesional hemorrhage. The NIR imaging characteristics of two other TVT nodules and a metastatic lymph node were retrospectively shown to be different from those of the regressing tumor and the cyst. Transrectal US-integrated spectral optical tomography seems to enable longitudinal monitoring of intra-lesional hemoglobin content and oxygenation of lesions in canine prostate.

Acknowledgement

The study was supported in part by DOD Prostate Cancer Research Program through an award #W81XWH-07-1-0247, an endowment fund to Kenneth E. Bartels from the Kerr Foundation, Oklahoma City, Oklahoma, and resources made available by National Cancer Institute through a subcontract of research grant R44 CA096153-03.

References

1. Jemal, A., Siegel. R., Xu. J., Ward. E. Cancer statistics, 2010. *CA Cancer J Clin 60*, 277-300 (2010).
2. Powers, W. E., Tolmach, L. J. A multicomponent x-ray survival curve for mouse lymphosarcoma cells irradiated in vivo. *Nature 197*, 710-711 (1963).
3. Shweiki, D., Itin, A., Soffer, D., Keshet, E. Vascular endothelial growth factor induced by hypoxia may mediate hypoxia-initiated angiogenesis. *Nature 359*, 843-845 (1992).
4. Kunz, M., Hartmann, A., Flory, E., Toksoy, A., Koczan, D., Thiesen, H. J., Mukaida, N., Neumann, M., Rapp, U. R., Bröcker, E. B., Gillitzer, R. Anoxia-induced up-regulation of interleukin-8 in human malignant melanoma. A potential mechanism for high tumor aggressiveness. *Am J Pathol 155*, 753-763 (1999).
5. Höckel, M., Schlenger, K., Höckel, S., Aral, B., Schäffer, U., Vaupel, P. Tumor hypoxia in pelvic recurrences of cervical cancer. *Int J Cancer 79*, 365-369 (1998).
6. Sundfør, K., Lyng, H., Rofstad, E. K. Tumour hypoxia and vascular density as predictors of metastasis in squamous cell carcinoma of the uterine cervix. *Br J Cancer 78*, 822-827 (1998).
7. Movsas, B., Chapman, J. D., Horwitz, E. M., Pinover, W. H., Greenberg, R. E., Hanlon, A. L., Iyer, R., Hanks, G. E. Hypoxic regions exist in human prostate carcinoma. *Urology 53*, 11-18 (1999).
8. Yu, G., Durduran, T., Zhou, C., Zhu, T. C., Finlay, J. C., Busch, T. M., Malkowicz, S. B., Hahn, S. M., Yodh, A. G. Real-time in situ monitoring of human prostate photodynamic therapy with diffuse light. *Photochem Photobiol 82*, 1279-1284 (2006).
9. Leith, J. T., Quaranto, L., Padfield, G., Michelson, S., Hercbergs, A. Radiobiological studies of PC-3 and DU-145 human prostate cancer cells: x-ray sensitivity in vitro and hypoxic fractions of xenografted tumors in vivo. *Int J Radiat Oncol Biol Phys 25*, 283-287 (1993).
10. Vukanovic, J., Isaacs, J. T. Human prostatic cancer cells are sensitive to programmed (apoptotic) death induced by the antiangiogenic agent linomide. *Cancer Res 55*, 3517-3520 (1995).
11. Tatum, J. L., Kelloff, G. J., Gillies, R. J., Arbeit, J. M., Brown, J. M., Chao, K. S., Chapman, J. D., Eckelman, W. C., Fyles, A. W., Giaccia, A. J., Hill, R. P., Koch, C. J., Krishna, M. C., Krohn, K. A., Lewis, J. S., Mason, R. P., Melillo, G., Padhani, A. R., Powis, G., Rajendran, J. G., Reba, R., Robinson, S. P., Semenza, G. L., Swartz, H. M., Vaupel, P., Yang, D., Croft, B., Hoffman, J., Liu, G., Stone, H., Sullivan, D. Hypoxia: importance in tumor biology, noninvasive measurement by imaging, and value of its measurement in the management of cancer therapy. *Int J Radiat Biol 82*, 699-757 (2006). Review.

12. Janssen, H. L., Haustermans, K. M., Balm, A. J., Begg, A. C. Hypoxia in head and neck cancer: how much, how important? *Head Neck 27*, 622-638 (2005). Review.
13. Movsas, B., Chapman, J. D., Hanlon, A. L., Horwitz, E. M., Pinover, W. H., Greenberg, R. E., Stobbe, C., Hanks, G. E. Hypoxia in human prostate carcinoma: an Eppendorf PO2 study. *Am J Clin Oncol 24*, 458-461 (2001).
14. Jöbsis, F. F. Noninvasive, infrared monitoring of cerebral and myocardial oxygen sufficiency and circulatory parameters. *Science 198*, 1264-1267 (1977).
15. Tromberg, B. J., Pogue, B. W., Paulsen, K. D., Yodh, A. G., Boas, D. A., Cerussi, A. E. Assessing the future of diffuse optical imaging technologies for breast cancer management. *Med Phys 35*, 2443-2451 (2008).
16. Zhu, Q., Tannenbaum, S., Kurtzman, S. H. Optical tomography with ultrasound localization for breast cancer diagnosis and treatment monitoring. *Surg Oncol Clin N Am 16*, 307-321 (2007). Review.
17. Gulsen, G., Birgul, O., Unlu, M. B., Shafiiha, R., Nalcioglu, O. Combined diffuse optical tomography (DOT) and MRI system for cancer imaging in small animals. *Technol Cancer Res Treat 5*, 351-363 (2006).
18. Pu, Y., Wang, W. B., Tang, G. C., Zeng, F., Achilefu, S., Vitenson, J. H., Sawczuk, I., Peters, S., Lombardo, J. M., Alfano, R. R. Spectral polarization imaging of human prostate cancer tissue using a near-infrared receptor-targeted contrast agent. *Technol Cancer Res Treat 4*, 429-436 (2005).
19. Cho, H., Ackerstaff, E., Carlin, S., Lupu, M. E., Wang, Y., Rizwan, A., O'Donoghue, J., Ling, C. C., Humm, J. L., Zanzonico, P. B., Koutcher, J. A. Noninvasive multimodality imaging of the tumor microenvironment: registered dynamic magnetic resonance imaging and positron emission tomography studies of a preclinical tumor model of tumor hypoxia. *Neoplasia 11*, 247-259 (2009).
20. Jiang, Z., Holyoak, G. R., Bartels, K. E., Ritchey, J. W., Xu, G., Bunting, C. F., Slobodov, G., Piao, D. *In vivo* trans-rectal ultrasound coupled near-infrared optical tomography of a transmissible venereal tumor model in the canine pelvic canal. *J Biomed. Opt Lett 14*, 030506-1-030506-3 (2009).
21. Jiang, Z., Piao, D., Holyoak, G. R., Ritchey, J. W., Bartels, K. E., Slobodov, G., Bunting, C. F., Krasinski, J. S. Trans-rectal ultrasound-coupled spectral optical tomography of total hemoglobin concentration enhances assessment of the laterality and progression of a transmissible venereal tumor in canine prostate. *Urology 77*, 237-242 (2011).
22. Zhu, Q. Optical tomography with ultrasound localization: initial clinical results and technical challenges. *Technol Cancer Res Treat 4*, 235-244 (2005).
23. Prier, J. E., Brodey, R. S. Canine neoplasi. A prototype for human cancer study. *Bull World Health Organ, 29*, 331-344 (1963). Review.
24. Hill, D. L., Yang, T. J., Wachtel, A. Canine transmissible venereal sarcoma: tumor cell and infiltrating leukocyte ultrastructure at different growth stages. *Vet Pathol 21*, 39-45 (1984).
25. Fenton, M. A., Yang, T. J. Role of humoral immunity in progressive and regressive and metastatic growth of the canine transmissible venereal sarcoma. *Oncology 45*, 210-213 (1988).
26. Santos, F. G. A., Vasconcelos, A. C., Nunes, J. E. S., Cassali, G. D., Paixão, T. A., Martins, A. S., Silva, S. S., Martins, R. F., Moro, L. Apoptosis in the transplanted canine transmissible venereal tumor during growth and regression phases. *Arq Bras Med Vet Zootec 60*, 607-612 (2008).
27. Pérez, J., Day, M. J., Mozos, E. Immunohistochemical study of the local inflammatory infiltrate in spontaneous canine transmissible venereal tumour at different stages of growth. *Vet Immunol Immunopathol 64*, 133-147 (1998).
28. Corlu, A., Durduran, T., Choe, R., Schweiger, M., Hillman, E. M. C., Arridge, S. R., Yodh, A. G. Uniqueness and wavelength optimization in continuous-wave multispectral diffuse optical tomography. *Opt Lett 28*, 2339-2341 (2003).
29. Xu, G., Piao, D., Bunting, C. F., Dehghani, H. Direct-current-based image reconstruction versus direct-current included or excluded frequency-domain reconstruction in diffuse optical tomography. *Appl Opt 49*, 3059-3070 (2010).
30. Li, A., Zhang, Q., Culver, J. P., Miller, E. L., Boas, D. A. Reconstructing chromosphere concentration images directly by continuous-wave diffuse optical tomography. *Opt Lett 29*, 256-258 (2004).
31. Hayes, M. D., Vanzant, E. S., Stombaugh, T. S., Gates, R. S. Comparison of bovine blood absorption coefficients to human curves. *Livestock Environment VIII Proceedings*, 981-5 (2008).
32. Forlani, L., Ioppolo, C., Antonini, E. Calorimetric studies of oxyhemoglobin dissociation. I. Reaction of sodium dithionite with oxygen. *J Inorg Biochem 20*, 147-155 (1984).
33. Nak, D., Nak, Y., Cangul, I. T., Tuna, B. A clinico-pathological study on the effect of vincristine on transmissible venereal tumour in dogs. *J Vet Med A Physiol Pathol Clin Med 52*, 366-370 (2005).
34. Kanick, S. C., van der Leest, C., Djamin, R. S., Janssens, A. M., Hoogsteden, H. C., Sterenborg, H. J., Amelink, A., Aerts, J. G. Characterization of mediastinal lymph node physiology in vivo by optical spectroscopy during endoscopic ultrasound-guided fine needle aspiration. *J Thorac Oncol 5*, 981-987 (2010).
35. Li, A., Liu, J., Tanamai, W., Kwong, R., Cerussi, A. E., Tromberg, B. J. Assessing the spatial extent of breast tumor intrinsic optical contrast using ultrasound and diffuse optical spectroscopy. *J Biomed Opt 13*, 030504 (2008).
36. Chang, Y. H., Chuang, C. K., Ng, K. F., Liao, S. K. Coexistence of a hemorrhagic cyst and carcinoma in the prostate gland. *Chang Gung Med J 28*, 264-267 (2005).
37. Galosi, A. B., Montironi, R., Fabiani, A., Lacetera, V., Gallé, G., Muzzonigro, G. Cystic lesions of the prostate gland: an ultrasound classification with pathological correlation. *J Urol 181*, 647-657 (2009).

Received: June 3, 2011; Revised: July 31, 2011;
Accepted: August 16, 2011